

Reverse engineering of the Xmon qubits

May 24, 2017

Contents

1	Theoretical introduction	3
1.1	Superconducting microwave coplanar waveguide resonators	3
1.1.1	Equations for quality factors	3
	The lumped-element model of a coplanar waveguide resonator	4
1.1.2	S-parameters for lines with resonators	5
	Notch (shunting) design	6
	Embedded (series) design	7
1.1.3	Time-resolved response	8
1.2	Circuit QED with transmon qubits	12
1.2.1	Transmon	12
1.2.2	Transmon eigenproblem	13
1.2.3	Hamiltonian of the transmon-resonator system	15
1.2.4	Energy spectrum of the transmon-resonator system	17
1.3	Dynamics	19
1.3.1	Driving of an isolated transmon	19
	Approximate solution for two-level dynamics	20
	Time-dependent perturbation theory	22
	Numerical solution for two-level dynamics	23
	Numerical solution for two-photon dynamics	24
1.3.2	Relaxation dynamics (driven and undriven)	25
1.3.3	Linewidth dependence on drive power	25

Chapter 1

Theoretical introduction

1.1 Superconducting microwave coplanar waveguide resonators

1.1.1 Equations for quality factors

The total quality factor of a microwave transmission line resonator (TLR) Q_l (loaded quality factor) can be calculated as a sum of two parts – the internal and external quality factors. The internal quality factor Q_i describes how excitations leave the resonator in the absence of coupling to any external circuitry, so damping in this case comes from the internal defects (i.e. resonant two-level systems) in the resonator itself. When, however, the resonator is coupled to the external circuitry having some active resistance, the damping is enhanced and the total Q-factor is reduced according to the following expression:

$$Q_l^{-1} = Q_i^{-1} + Q_e^{-1}, \quad (1.1.1)$$

where Q_e is determined by the value of the externally connected resistance and the way of its connection.

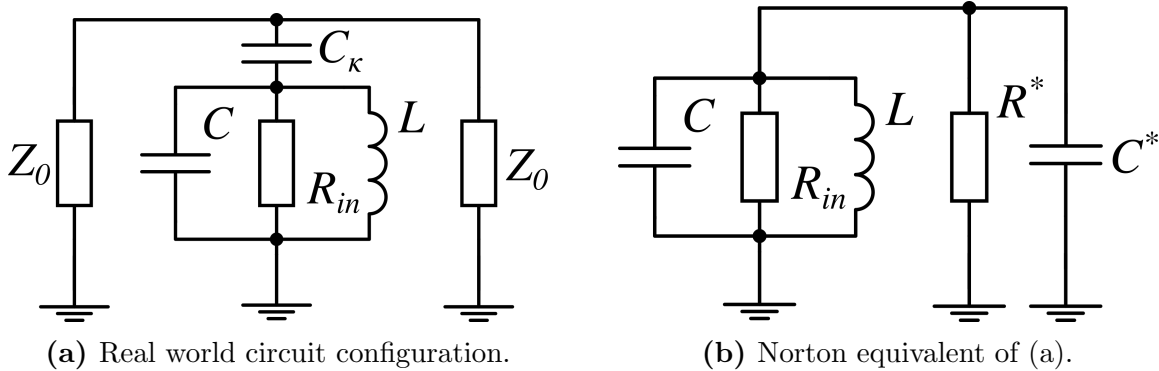


Figure 1.1: Equivalent circuit for a $\lambda/4$ TLR, capacitively coupled to the transmission line near resonance.

A common way of measuring a resonator is to couple it capacitively to an external transmission line. The coupling on the equivalent scheme of the circuit is represented as C_κ , as depicted in Fig. 1.1 (a). An infinite/properly terminated transmission line can be represented as a single resistance of Z_0 Ohms, where Z_0 is the line's wave impedance; thus, two such resistances are added to the both sides of the resonator circuit. The resonators are of $\lambda/4$ type, so the equivalent for each of them is a parallel RLC oscillator (see below), where C and L are, respectively, its equivalent capacitance and inductance and $R = R_{in}$ characterises the internal dissipation. Its $Q_i = \omega_0 C R_{in}$ where $\omega_0 = \sqrt{1/LC}$ can be calculated from the definition when no external impedance is connected.

The external Q-factor can be derived in a bit more complicated way.¹ We can transform the circuit from the Fig. 1.1 (a) to explicitly include the external parameters into the internal ones. To do so one needs to convert the series connection of the coupling capacitor and the characteristic impedances into parallel, as done on the Fig. 1.1 (b). The R^* and C^* impedances should be chosen in such a way that total impedance of the external circuit is the same as before the transformation:

$$R^* = \frac{1 + \omega^2 C_\kappa^2 (Z_0/2)^2}{\omega^2 C_\kappa^2 (Z_0/2)^2}, \quad (1.1.2)$$

$$C^* = \frac{C_\kappa}{1 + \omega^2 C_\kappa^2 (Z_0/2)^2} \approx C_\kappa \text{ (in our case)}. \quad (1.1.3)$$

From this and Fig. 1.1 (b) it is simple to write down the expression for the internal, external and loaded quality factors:

$$Q_i = \omega(C + C^*)R_{in}, \quad (1.1.4)$$

$$Q_e = \omega(C + C^*)R^*, \quad (1.1.5)$$

$$Q_l = \omega(C + C^*) \frac{1}{1/R^* + 1/R_{in}}. \quad (1.1.6)$$

The above expressions readily justify (1.1.1). The values been used in the simulations are: $C = 350$ fF, $L = 2$ nH, $R_{in} = 10^7$ Ohm, $Z_0 = 50$ Ohm.

The lumped-element model of a coplanar waveguide resonator

A $\lambda/4$ coplanar waveguide (CPW) resonator near a resonance is equivalent to a lumped-element parallel resonance circuit, as in Fig. 1.1. L and C for the lumped-element models of CPW resonators are bound not only by the resonance frequency condition $\omega_0 = 1/\sqrt{LC}$ but also by the geometry of the waveguide or, in other words, C' and L' – the transmission line capacitance and inductance per unit length. To show this, one would write down the impedance of the CPW resonator near its resonance frequency ω_0 and compare it to the lumped-element one's.² Such comparison leads to the following expressions:

$$R_{in} = \frac{Z_0}{\alpha l}, \quad C = \frac{\pi}{4\omega_0 Z_0},$$

where l is the resonator length, $Z_0 = \sqrt{L'/C'}$ is the wave resistance and α is the decay constant of the line. Then the resonance condition for the wavelength ($\lambda = 4l$) is used along

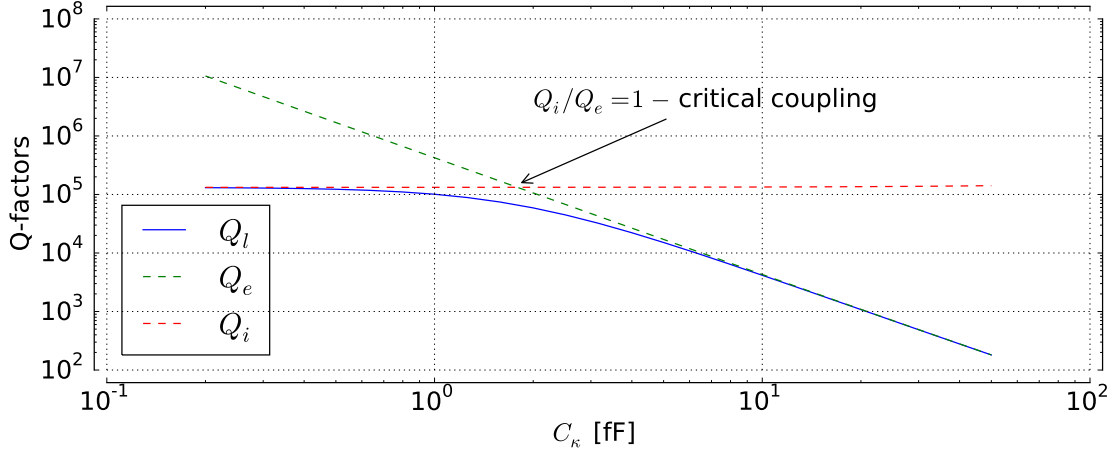


Figure 1.2: Q-factors dependence on C_κ according to (1.1.6).

with the phase velocity expression $v_{ph} = 1/\sqrt{L'C'}$:

$$\omega_0 = \frac{2\pi v_{ph}}{\lambda} = \frac{\pi v_{ph}}{2l} \Rightarrow C = \frac{C'l}{2}.$$

For the inductance one can use $L = 1/\omega_0^2 C = 8l L'/\pi^2$. Finally, the expressions for C' and L' :

$$C' = 4\epsilon_0\epsilon_{eff} \frac{K(k_0)}{K(k'_0)}, \quad L' = \frac{\mu_0}{4} \frac{K(k'_0)}{K(k_0)},$$

where $K(x)$ is the complete elliptic integral of the first kind, $\epsilon_{eff} = \frac{1+\epsilon_{substrate}}{2}$, $k_0 = \frac{W}{W+2G}$ where W is the width of the hotwire and G is the width of the gaps and finally $k'_0 = \sqrt{1 - k_0^2}$.

1.1.2 S-parameters for lines with resonators

Typically, a microwave device under test (DUT) is tested with a vector network analyser, which measures the scattering matrix (S-matrix) of the DUT. So below we will discuss the S-matrix for two different coupling configurations. Generally, a two-port DUT can be drawn like in Fig. 1.3. For such system it is possible to calculate different 2 by 2 matrices, which bind together voltages and currents on the ports 1 and 2. S-matrix also has 4 values, named S-parameters.

To calculate S-parameters one needs to treat voltages and currents, which can be calculated from Kirchhoff's laws, as a sum of the incident and reflected components (“+” corresponds to the incident wave and “−” to the reflected wave):

$$V_{1,2} = V_{1,2}^+ + V_{1,2}^-,$$

$$I_{1,2} = I_{1,2}^+ + I_{1,2}^- = \frac{V_{1,2}^+ - V_{1,2}^-}{Z_0},$$

where the difference in the second expression arises from telegrapher's equations. Solving these with respect to incident and reflected components, one can get

$$V_{1,2}^\pm = \frac{1}{2}(V_{1,2} \pm Z_0 I_{1,2}).$$

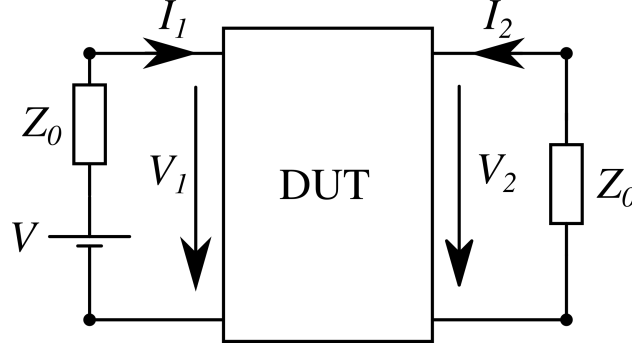


Figure 1.3: A scheme for the two-port network.

From this, finally, S-parameters are defined:

$$\begin{pmatrix} V_1^- \\ V_2^- \end{pmatrix} = \begin{pmatrix} S_{11} & S_{12} \\ S_{21} & S_{22} \end{pmatrix} \begin{pmatrix} V_1^+ \\ V_2^+ \end{pmatrix}. \quad (1.1.7)$$

However, it's often more convenient to use indirect methods of calculating S-parameters, for example, to extract them from $ABCD$ -matrix.

Notch (shunting) design

For a notch design one can treat the resonator as a shunt in the transmission line as in Fig. 1.4. Except than by the definition (1.1.7) there are two other ways to calculate the S-matrix. First one is intuitive but is not valid for every configuration. Transmission and reflection parameters are defined³ below (the second formula is valid only for the “shunt” configuration, no series elements are allowed in the line):

$$\Gamma = \frac{Z_{eff} - Z_0}{Z_{eff} + Z_0} = S_{11} = S_{22}, \quad (1.1.8)$$

$$T = \frac{2Z_{eff}}{Z_{eff} + Z_0} \stackrel{!}{=} S_{21} = S_{12}, \quad (1.1.9)$$

where $Z_{eff} = Z_0 || Z_{shunt}$, $Z_{shunt} = \frac{1}{i\omega C_\kappa} + 1/i\omega C || R_{in} || i\omega L$ and the equalities between S-parameters hold due to the symmetry.

Another way is to calculate $ABCD$ matrix or impedance matrix and convert it to the S-matrix with corresponding formulae.² In the “shunted” case from both this approaches the simplified expressions for the S-parameters follow:

$$S_{11} = -\frac{Z_0}{1 + 2Z_{shunt}/Z_0} = S_{22}, \quad (1.1.10)$$

$$S_{21} = \frac{1}{1 + Z_0/2Z_{shunt}} = S_{12}. \quad (1.1.11)$$

The second expression is plotted in Fig. 1.5 along with the loaded quality factors calculated with (1.1.6) and with the “3db”-method ($Q_L \approx \omega_0/\Delta\omega_{3db}$). It can be seen that with increase of capacitance resonance frequency and Q_l decrease, which is expected according to Fig. 1.1 (b) and (1.1.3).

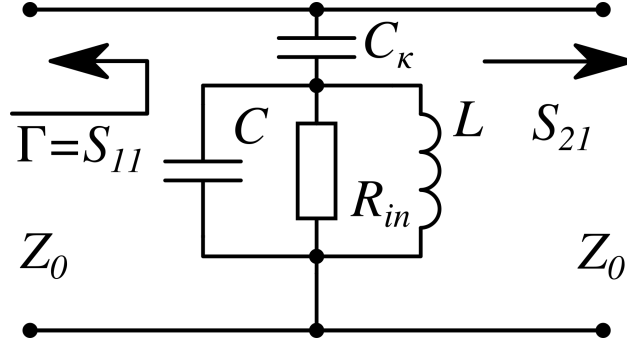


Figure 1.4: The shunted transmission line. This is Fig. 1.1 (a) from the observer's point of view.

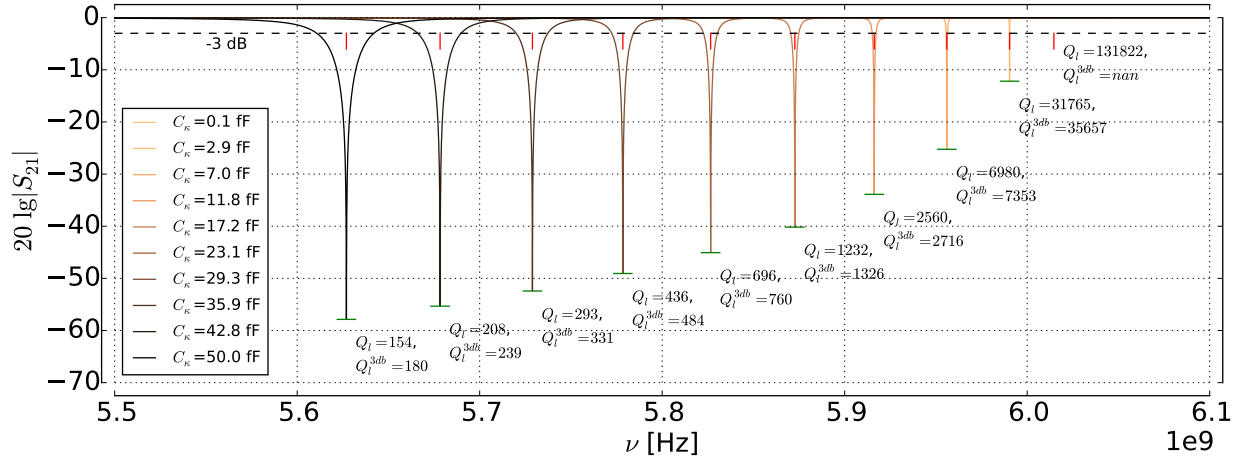


Figure 1.5: $|S_{21}|$ parameters from (1.1.11) for different coupling strengths. The loaded quality factors are calculated with (1.1.6) and with the “3db”-method. The red dashes show the values of expression $\sqrt{1/L(C + C_k)}$ according to Fig. 1.1 (b), the green ones show the theoretically predicted depths.

In Fig. 1.5 the resonance frequencies calculated from the equivalent circuit in Fig. 1.1 (b) are shown along with the analytically calculated depths of the peaks:

$$\min_f |S_{21}| = \frac{2L(C + C_k)}{\sqrt{C_k^2 L Z_0^2 (C + C_k) + (2(C + C_k)L + C_k^2 R_{in} Z_0)^2}}. \quad (1.1.12)$$

Embedded (series) design

For the embedded resonator it's possible to draw a similar equivalent circuit as for the “shunt” design.¹ It is depicted in Fig. 1.6.

For this kind of connection of the resonator to the transmission line (1.1.9) is now not valid (however, (1.1.8) still holds). To calculate transmission in this case one may find the transmission matrix and then convert it to the S-matrix or use Kirchhoff's laws and (1.1.7).

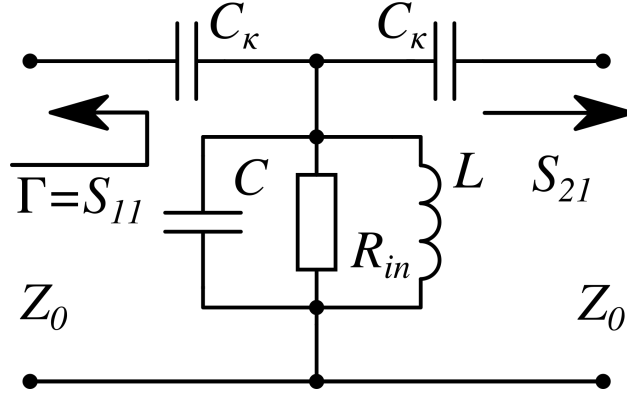


Figure 1.6: The equivalent circuit for the embedded resonator.

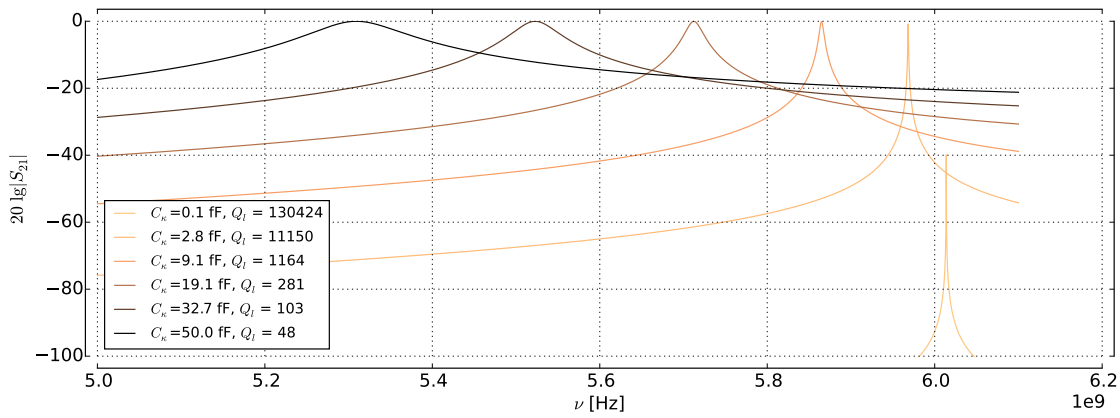


Figure 1.7: S_{21} for the series configuration. Loaded Q-factors were calculated via analytic expression similar to (1.1.6).

For studied case one can get the following $ABCD$ -matrix²

$$\hat{T} = \begin{pmatrix} A & B \\ C & D \end{pmatrix} = \begin{pmatrix} 1 + \frac{1/i\omega C_K}{Z_{res}} & 2/i\omega C_K - \frac{\omega^2 C_K^2}{Z_{res}} \\ 1/Z_{res} & 1 + \frac{1/i\omega C_K}{Z_{res}} \end{pmatrix}, \quad (1.1.13)$$

where $Z_{res} = R_{in} || i\omega L || 1/i\omega C$. The corresponding S_{21} is plotted in Fig. 1.7, calculated as²

$$S_{21} = \frac{2}{A + B/Z_0 + CZ_0 + D}. \quad (1.1.14)$$

1.1.3 Time-resolved response

As soon as the spectral characteristics of the resonator are established it is possible to calculate its response when a pulse of finite width is applied to it. The shape that the pulse will have after it has interacted with the resonator is important when pulsed readout is considered in time-resolved qubit measurements.

In this section we will only discuss the notch-type resonator and only the transmission of the pulses; however, the numerical method that will be used can be straightforwardly

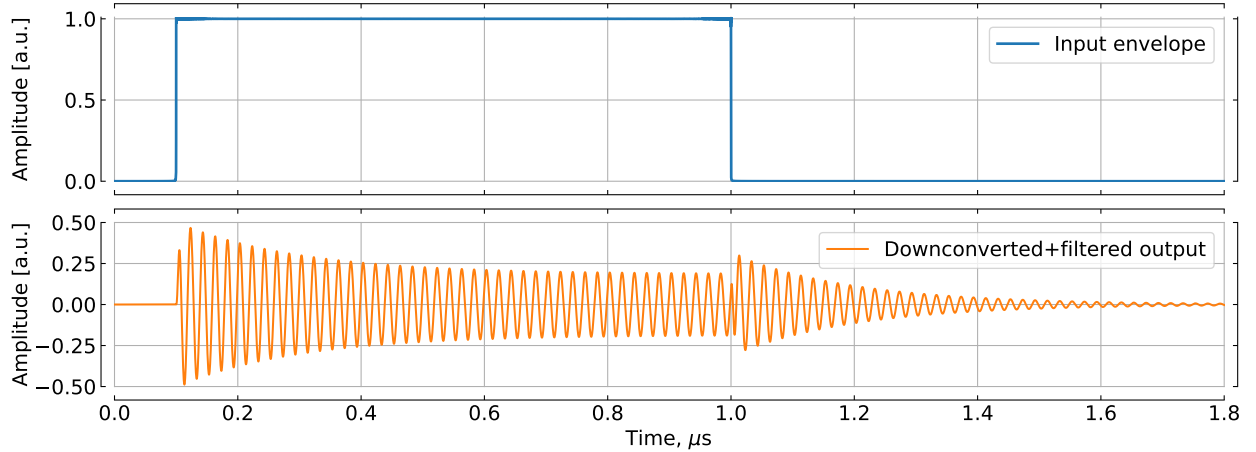


Figure 1.8: Calculated shape of the resonant pulse transmitted through the notch-type resonator ($f_0 = 6$ GHz, $Q_e = 6 \cdot 10^3$, $Q_i = 10^4$). Due to very high frequency of the input pulse only its envelope extracted using Hilbert transform is presented. Output pulse is obtained by simulating a downconversion: the UHF pulse after the resonator was multiplied by a sine wave detuned by low intermediate frequency of 50 MHz and then filtered with a digital 100 MHz low-pass filter. This procedure is very useful as it allows to visualize the phase of the UHF signal and, moreover, exactly models that what occurs in experiment.

extended to other cases. It consists of three steps: calculate the discrete Fourier transform (DFT) for the input pulse, multiply it by the required complex S-parameter for each frequency (negative and positive frequencies should be multiplied in the same way), and finally perform the inverse discrete Fourier transform.

We will use the following expression for the complex S_{21} of an ideal notch-type resonator:⁴

$$S_{21}(\omega) = 1 - \frac{Q_l/Q_e}{1 + 2iQ_l(\omega/\omega_0 - 1)}.$$

Then we perform the following operation on the input rectangular pulse $x(t)$ to obtain the transformed signal $x'(t)$:

$$x'(t) = \frac{1}{2\pi} \int_{-\infty}^{+\infty} e^{i\omega t} S_{21}(-\omega_r, \omega) S_{21}(\omega_r, \omega) \int_{-\infty}^{+\infty} e^{-i\omega t} x(t) dt d\omega.$$

Using DFT this procedure becomes a little bit more tricky as it requires careful tracking of the indices and asymmetries that emerge from discreteness. The results of such calculation are presented in Fig. 1.8 and Fig. 1.9.

Fig. 1.8 shows what happens with a rectangular pulse with resonant carrier frequency when it comes through the notch-type resonator. The output pulse has a peculiar shape that can be divided in time into three parts: the “ring-up” part, the steady state part, and the “ring-down” part. The first part is an exponent-like transient with rate determined by both Q_e and Q_i , the steady state part determines the amplitude and phase of the transmitted signal in the continuous wave measurements, and the third part is simply an exponential decay

of the excitation inside the resonator with rate $\kappa = \omega_0/Q_l$ at frequency ω_0 . Additionally, the shape of the pulse does not depend on power; however, the steady-state amplitude of the wave inside it (or the number of photons in the quantum limit) does. So in the experiment length of the pulses or the spacing between them do not define the number of photons inside the resonator as long as they are long enough to drive the resonator into the steady state.

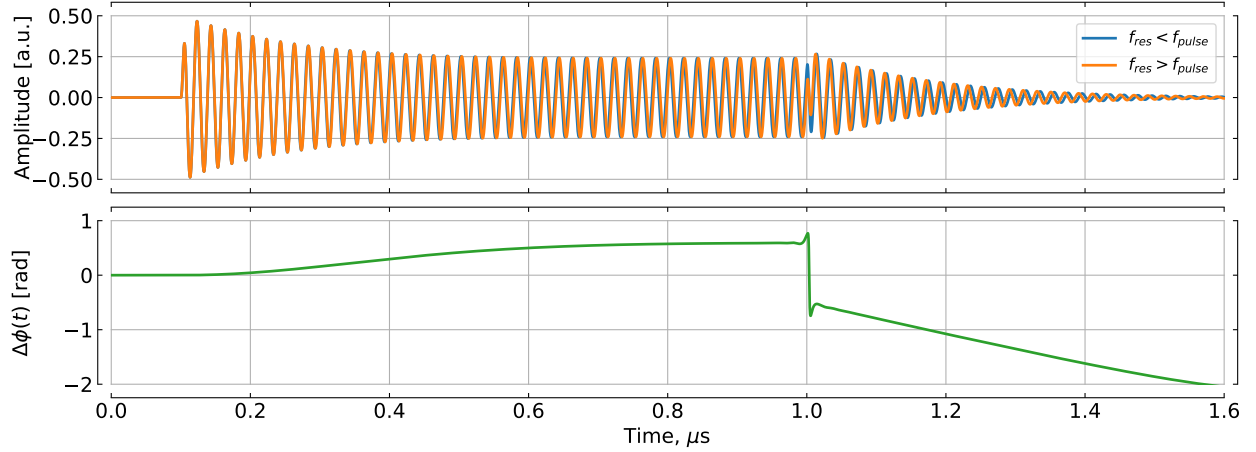


Figure 1.9: Simulated response for slightly off-resonant interaction (as in dispersive readout). The input pulses were identical, but the resonance frequency was either higher (orange) or lower (blue) than their carrier frequency. Here pulse carrier was 6 GHz, and resonator frequencies were 6.0005 GHz and 5.9995 GHz, respectively. The difference between instantaneous phases calculated from Hilbert transform is also presented.

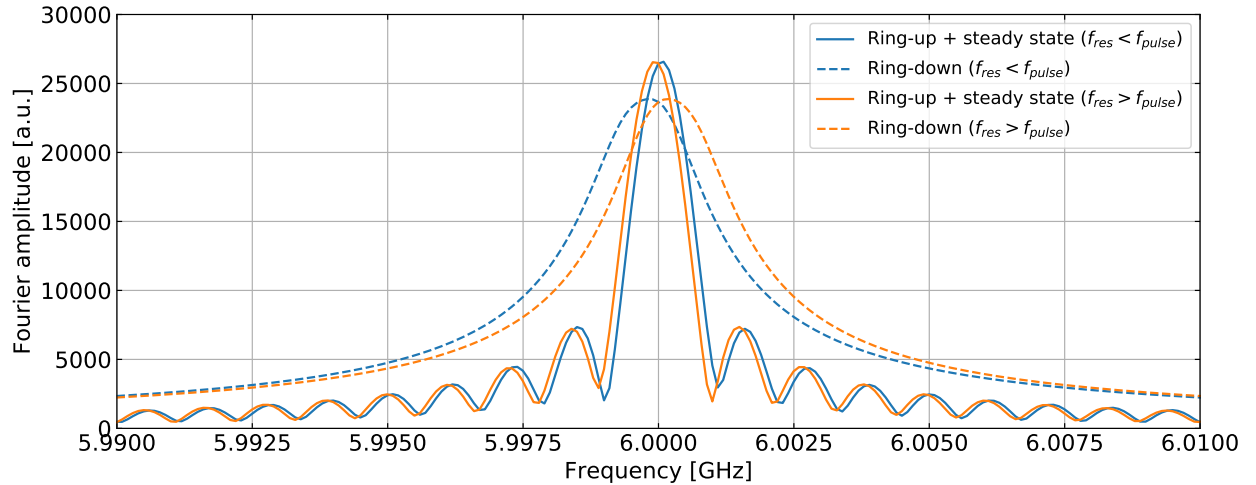


Figure 1.10: Separate DFTs for two different pulse parts. Same two resonator frequency cases as in Fig. 1.9 are displayed in blue and orange, respectively. Notice that the “ring-down” parts are close to resonator frequency in contrast to the “ring-up” and steady state parts which are closer to the pulse carrier frequency.

In Fig. 1.9 two output pulses obtained from the same input rectangular pulse are presented for two different cases of resonance frequency above and below the pulse carrier

frequency. It can be seen that during the first 100 ns the two output pulses are nearly identical in their amplitude and phase. Then, gradually, the phase difference between the pulses begins to accumulate until it reaches saturation in the steady state. Then the “ring-down” part begins and the phase difference changes the sign abruptly and then continues to accumulate. This behaviour is due to the fact that, firstly, the resonator has to accumulate the amplitude at least comparable to the amplitude of the incident wave to influence it in any way, i.e. to shift its phase. This is why the first part is called “ring-up”. Then it reaches the steady state where the phase difference is constant and equals the value one would observe on a vector network analyser. Finally, the phase difference between the “ring-down” parts of the two pulses is caused simply by the difference between the resonator frequencies (after the end of the pulse the resonator experiences free oscillations).

1.2 Circuit QED with transmon qubits

1.2.1 Transmon

Before turning to the circuit QED with transmons, it is necessary first to describe the transmon itself. This type of qubit has been introduced⁵ in 2007 by J. Koch et al., and since then was used extensively in many groups around the world.

A transmon is a Cooper pair box where the Josephson junction (JJ) capacitance is extended with a shunt capacitor inserted in parallel with the junction (see Fig. 1.11 (a),(b)) which leads to the reduction of the capacitive energy of the circuit. The reason for this modification is that it exponentially suppresses the *charge dispersion*, that is, the dependence of the energy levels of the qubit on the induced charge, while maintaining a sufficient anharmonicity of the circuit. This means that such qubits are becoming immune to dephasing from the charge noise ubiquitous on the chip due to dipole defects. Recently, flux qubits with increased coherence due to a capacitively shunted smaller junction were also demonstrated.⁶

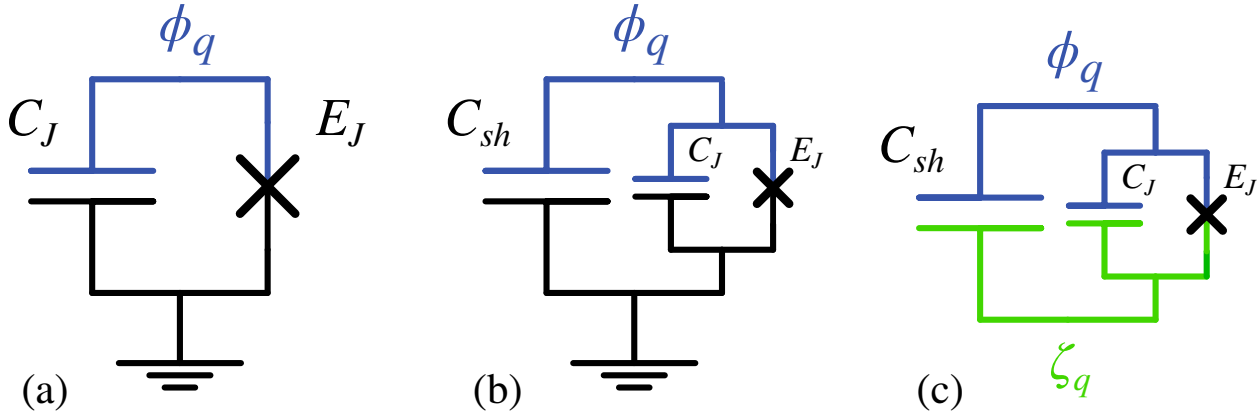


Figure 1.11: Transition from a charge qubit to a transmon. Colours and Greek letters denote the degrees of freedom of the systems. (a) Cooper pair box which is simply a JJ connecting a small superconducting island with the ground. (b) Transmon which is different from (a) just by the additional shunting capacitor C_{sh} in parallel to the junction, i.e. larger island with dominating capacitance to the ground. (c) Floating transmon, a variation of the design (b) which is not connected to the ground and has two superconducting islands. The charge is saved in the system, so the two degrees of freedom can be reduced to one, $\phi_q - \zeta_q$.

Two versions of the transmon qubits exist (see Fig. 1.11 (b),(c)). The first has a single superconducting island which has some large (compared to the JJ) capacitance to the ground, and the second has two islands forming a capacitor. These two versions are exactly the same concerning the energy structure given that their electrical parameters are the same; however, the second type does not require the ground plane, and thus can be used in 3D waveguides or waveguide resonators.⁷ In the original transmon paper⁵ the second form was presented, and the first form was not mentioned. This led to the wide spread of the two-island transmons both in 3D and planar architectures which had many different shapes of the capacitors. For planar cQED this was an unnecessary complication as the calculation of the coupling for such qubits is much more complicated (see Appendix B of the Koch's paper). The

transmons of the first type (embedded in the ground plane) became popular after the work⁸ by the group of J. Martinis where they have demonstrated a coherent transmon with a single superconducting island.

Below we discuss the quantum mechanics of a transmon of the first type, as long as this is the type that was investigated in the experimental part. But, until we turn to coupling calculation the results for the two-island qubits are exactly the same. First of all, the Hamiltonian of the system depicted in Fig. 1.11 (b) is written down:

$$\hat{H}_{tr} = 4E_C \hat{n}^2 - E_J \cos \hat{\varphi}, \quad (1.2.1)$$

where $E_C = e^2/2C_\Sigma$, $C_\Sigma = C_J + C_{sh}$, $E_J = I_c \hbar/2e$ is the standard Josephson energy, \hat{n} is the number operator of excess cooper pairs on the island and $\hat{\varphi}$ is the phase difference operator across the junction (equal to the phase operator $\hat{\phi}$ of the single island or to the phase difference operator between two islands⁹). The phase-dependent part of this Hamiltonian can be transformed into charge representation. From the Euler's formula $\cos \hat{\varphi} = (e^{i\hat{\varphi}} + e^{-i\hat{\varphi}})/2$, the fact that n and φ are conjugate variables, i.e. $\langle \varphi | n \rangle = \psi_n(\varphi) = e^{in\varphi}$, the series expansion of the exponent and decomposition of the unity operator $\mathbb{1} = \int d\varphi |\varphi\rangle \langle \varphi|$, we obtain

$$\begin{aligned} e^{\pm i\hat{\varphi}} |n\rangle &= \sum_n \frac{\pm i\varphi}{k!} |n\rangle = \int d\varphi \sum_k \frac{(\pm i)^k \hat{\varphi}^k | \varphi \rangle}{k!} \langle \varphi | n \rangle \\ &= \int d\varphi e^{\pm i\varphi} e^{in\varphi} |\varphi\rangle = \int d\varphi |\varphi\rangle \langle \varphi | n \pm 1 \rangle \\ &= |n \pm 1\rangle. \end{aligned}$$

With this equality and the orthogonality of the $|n\rangle$ states, we can construct the operator $\cos \hat{\varphi}$:

$$\cos \hat{\varphi} = \frac{1}{2} \sum_n [|n+1\rangle \langle n| + |n-1\rangle \langle n|].$$

This representation allows straightforward numerical solution of different eigenproblems with transmons in the simple matrix form.

Another point that should be mentioned is the possibility of replacement of the single JJ in the transmon by a SQUID. This makes the transmon's energy spectrum tunable by external magnetic flux flowing through the loop of the SQUID. The dependence of the Josephson energy on the flux is then described by the following expression:⁵

$$E_J(\Phi_{ext}) = (E_{J1} + E_{J2}) \cos \left(\pi \frac{\Phi_{ext}}{\Phi_0} \right) \sqrt{1 + d^2 \tan^2 \left(\frac{\pi \Phi_{ext}}{\Phi_0} \right)},$$

where $d = \frac{E_{J1} - E_{J2}}{E_{J1} + E_{J2}}$ is the SQUID asymmetry. In this case the flux value which provides the largest possible E_J (for example, $\Phi_{ext} = 0$) is called *sweet spot* since in it the transmon is maximally insensitive to the flux noise.

1.2.2 Transmon eigenproblem

In this section the solution of the problem $\hat{H}_{tr}|m\rangle = E_m|m\rangle$ will be discussed. That is, it is necessary to find the eigenenergies and eigenstates of the transmon. As long as the

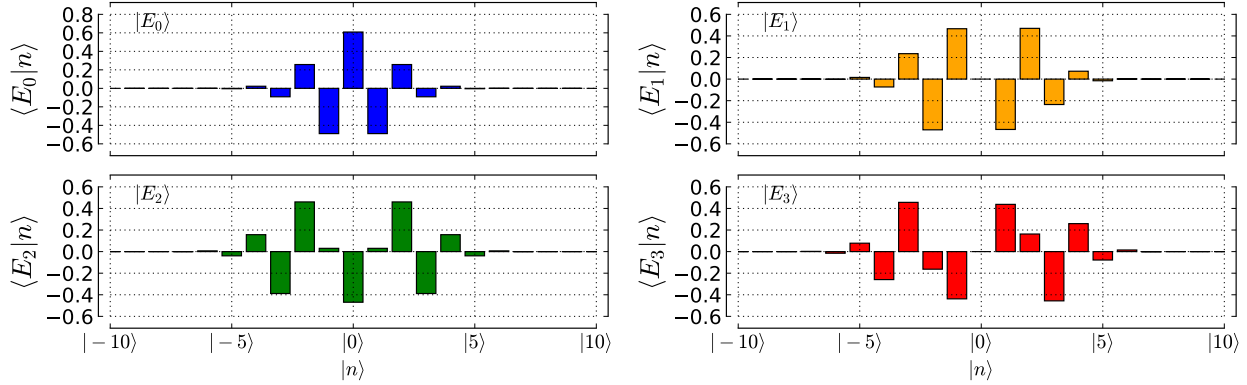


Figure 1.12: Eigenstates in charge representation for first four energy levels of the transmon. Note how the parity of the states is switched from even to odd and back with increasing m . This behaviour is the same for higher levels, too.

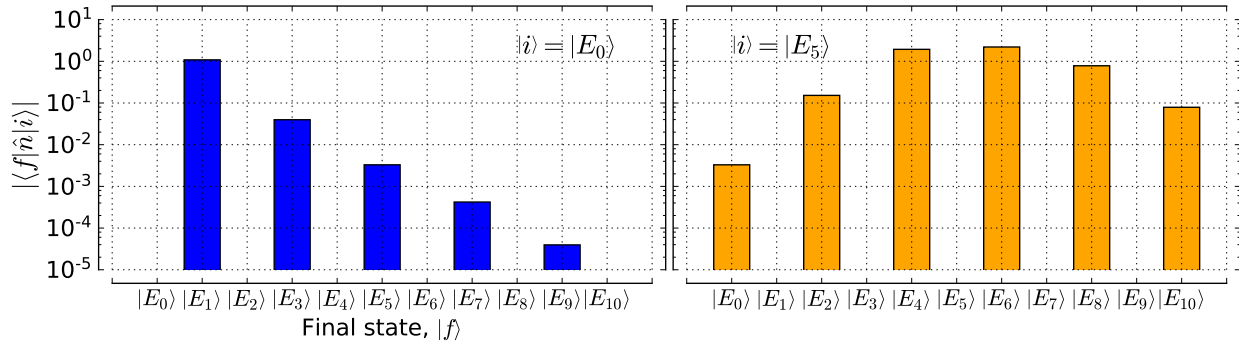


Figure 1.13: Some of the matrix elements of the \hat{n} operator. Note the linear decay of the matrix elements in the log scale over “distance” between states which means exponential suppression of the transition rates between them. This suppression is much more pronounced for low initial states than for the higher ones. Single-photon transitions between states of same parity are forbidden and because the corresponding matrix elements are zero.

transmon can be considered as a slightly anharmonic quantum oscillator, it is possible to calculate its energy spectrum perturbatively by expanding the cosine function in the (1.2.1) up to the fourth order term. This approach leads⁵ to the following energy structure (up to a constant offset):

$$E_m = m\sqrt{8E_J E_C} - \frac{E_C}{12}(6m^2 + 6m), \quad (1.2.2)$$

Additionally, numerically obtained eigenstates in charge basis for $m = 1..4$ are shown in Fig. 1.12. From this expression we can notice already that each subsequent transition frequency $\omega_{n-1,n}$ is reduced by the value of nE_C/\hbar , so we define the *anharmonicity* $\alpha = -E_C/\hbar$ of the transmon (in frequency units) which makes its level structure different from the harmonic oscillator’s, hence the name.

For convenience, below we will denote first energy levels as g, e, f, d . We will look at the expression (1.2.2) in detail. We need to find out what transition frequencies near transition ge ($\omega_{ge} = E_e - E_g = \sqrt{8E_J E_C} - E_C$) can be observed in the experiment, especially in case of a

Level	Energy	Transition	Frequency
g	0	ge	ω_{ge}
e	$\sqrt{8E_J E_C} - E_C$	$gf/2$	$\omega_{ge} - 0.5E_C$
f	$2\sqrt{8E_J E_C} - 3E_C$	$ef, gd/3$	$\omega_{ge} - E_C$
d	$3\sqrt{8E_J E_C} - 6E_C$	$ed/2$	$\omega_{ge} - 1.5E_C$
E_4	$4\sqrt{8E_J E_C} - 10E_C$	$fd, eE_4/3$	$\omega_{ge} - 2E_C$

Table 1.1: Energies and some transition frequencies for first 5 levels of the transmon calculated with (1.2.2).

non-zero thermal population of the first excited state and including multiphoton transitions.

The operator which is responsible for transmon excitation in case of capacitive coupling to the driving field (classical or quantized) is simply proportional to \hat{n} .⁵ So, to determine what transitions are allowed, it is very useful to look at the parity of the eigenstates of the transmon in n -representation in Fig. 1.12 and to recall that \hat{n} is itself odd. Obviously, \hat{n} can not induce transitions between states of same parity in a single-photon process as long as $\langle m|\hat{n}|m+2j\rangle = 0$, $j \in \mathbb{Z}$. Moreover, in general single-photon transitions between distant levels $m \rightarrow m+k$ where $k > 1$ are more or less suppressed¹⁰ even for the odd k (for large m this may be not exactly true, see Fig. 1.13 for exact numerically obtained data).

In Table 1.1 first five eigenenergies and frequencies of allowed transitions between them calculated with (1.2.2) are presented. The frequencies listed there are expected to appear on the spectral data in the experiment, and indeed they may be observed when the excitation power is high enough. We will discuss the oscillator strengths for these transitions calculated from perturbation theory and look at numerical simulations in the section 1.3 where quantum dynamics of our systems will be studied.

1.2.3 Hamiltonian of the transmon-resonator system

In this section one of the most important concepts in the area of superconducting quantum devices will be reviewed. It is the so-called *circuit QED* or *cQED*, i.e. circuit quantum electrodynamics of cavity quantum electrodynamics in electrical circuits.¹¹ The idea of cQED is to couple a superconducting qubit to an electric oscillator (which is usually a mode of a microwave transmission line resonator) to obtain many useful effects such as non-demolition readout,¹¹ Purcell decay protection,⁵ coupling of distant qubits,¹² single photon emission,¹³ etc.

With transmon qubits cQED approach is crucial since it is not possible to directly read out the transmon state neither with charge nor with flux based measurement apparatus since transmon eigenstates are electrically and magnetically neutral (at the sweet spot). However, the *dispersive readout*¹¹ of such qubits has now been proven to be very effective. Below we will calculate the spectrum of the transmon-oscillator system and find the transmon state-dependent dispersive shifts.

First of all, it is necessary to construct the full Hamiltonian for the transmon-oscillator system depicted in Fig. 1.14. We will use the results acquired by Bader¹⁴ and Koch.⁵ The

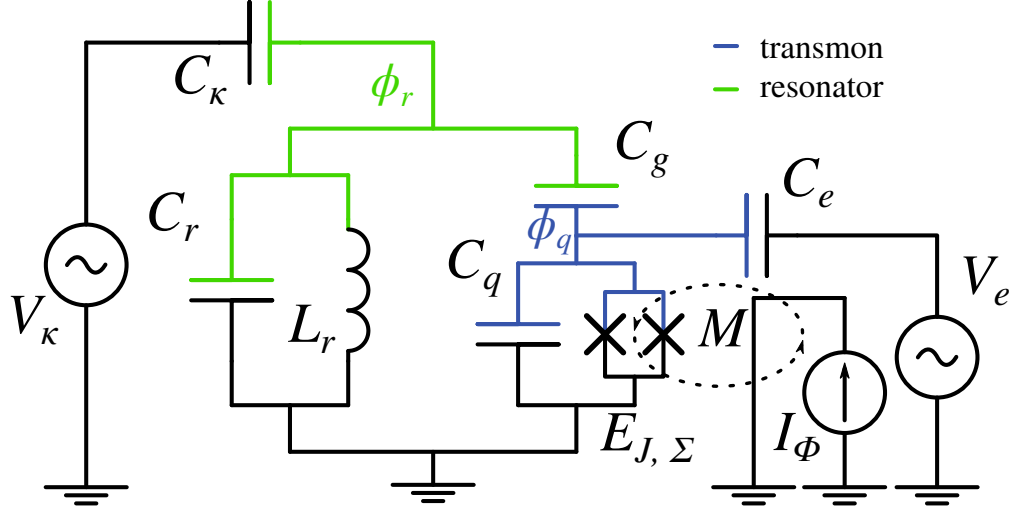


Figure 1.14: Equivalent circuit for coupled system of a tunable transmon qubit and a resonator. Colors show nodes (or branches) containing system's degrees of freedom according to M. Devoret's theory.⁹

system under study has two degrees of freedom; one from the resonator and one from the qubit. The coupling between the systems is achieved due to the presence of a capacitor C_g whose energy depends on both degrees of freedom. The Lagrangian of the circuit is then easy to write down, and with some calculations it is possible to obtain as well the quantized Hamiltonian for the compound circuit:

$$\begin{aligned}
 \hat{\mathcal{H}} &= \underbrace{\frac{\hat{\phi}_r^2}{2L_r} + \frac{(C_q + C_g)\hat{Q}_r^2}{2C_*^2}}_{\text{resonator}} + \underbrace{\frac{(C_g + C_\kappa + C_r)\hat{Q}_q^2}{2C_*^2} - E_J(\Phi_{ext}) \cos \frac{2e}{\hbar} \hat{\phi}_q + \frac{C_g \hat{Q}_r \hat{Q}_q}{C_*^2}}_{\text{qubit}} = \\
 &= \hbar\omega_r \hat{a}^\dagger \hat{a} \otimes \hat{\mathbb{1}}_q \quad (\hat{\mathcal{H}}_r) \\
 &+ 4E_C \hat{\mathbb{1}}_r \otimes \hat{n}^2 - \frac{E_J(\Phi_{ext})}{2} \hat{\mathbb{1}}_r \otimes \sum_{n=-\infty}^{+\infty} |n+1\rangle\langle n| + |n\rangle\langle n+1| \quad (\hat{\mathcal{H}}_q) \\
 &- 2e \frac{C_g}{C_*} \sqrt{\frac{\hbar\omega_r}{2(C_q + C_g)}} i(\hat{a}^\dagger - \hat{a}) \otimes \hat{n}, \quad (\hat{\mathcal{H}}_i)
 \end{aligned} \tag{1.2.3}$$

where

$$C_*^2 = C_q C_g + C_q C_\kappa + C_g C_\kappa + C_q C_r + C_g C_r,$$

$$\omega_r = 1/\sqrt{L_r C_*^2/(C_q + C_g)},$$

$$E_C = \frac{(C_g + C_\kappa + C_r)e^2}{C_*^2},$$

$$E_J(\Phi_{ext}) = E_{J,\Sigma} \cos(\Phi_{ext}/\Phi_0), \quad \Phi_{ext} = I_\Phi M.$$

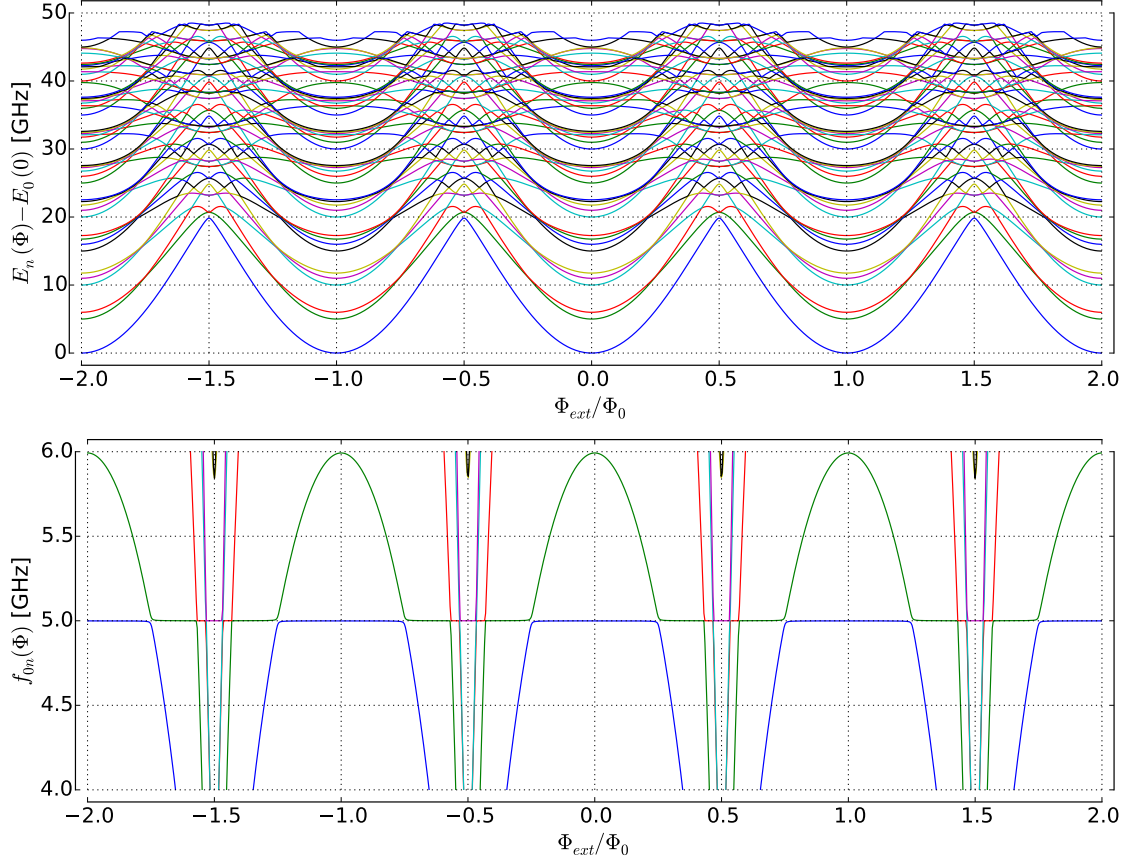


Figure 1.15: Energy structure and transition frequencies (from the ground state) of the transmon-resonator system depending on Φ_{ext} .

Presuming the coupling is not very strong ($C_g \ll C_q, C_r$) it is possible also to include simple time-dependent driving terms for both subsystems:

$$\begin{aligned}\hat{\mathcal{H}}_r^d(t) &= \frac{C_\kappa V_\kappa(t)}{C_r + C_\kappa} \hat{Q}_r \propto f_r(t) i(\hat{a}^\dagger - \hat{a}) \otimes \hat{\mathbb{1}}_q, \\ \hat{\mathcal{H}}_q^d(t) &= \frac{C_e V_e(t)}{C_q + C_e} \hat{Q}_q \propto f_q(t) \hat{\mathbb{1}}_r \otimes \hat{n},\end{aligned}\tag{1.2.4}$$

where $f_{q,r}(t)$ are the effective values of the drive magnitudes at time t .

1.2.4 Energy spectrum of the transmon-resonator system

Using QuTiP¹⁵ it is easy to solve the truncated matrix eigenproblem with the Hamiltonian (1.2.3). The results for the typical design values

$$C_\kappa = 5 \text{ fF}, \quad C_g = 2 \text{ fF}, \quad C_q = 90 \text{ fF}, \quad C_r = 500 \text{ fF}, \quad L_r = 2 \text{ nH},$$

$$E_{J,\Sigma} = (h\nu_q + E_C)^2 / 8E_C \text{ for } \nu_q = 6 \text{ GHz}$$

can be observed in Fig. 1.15.

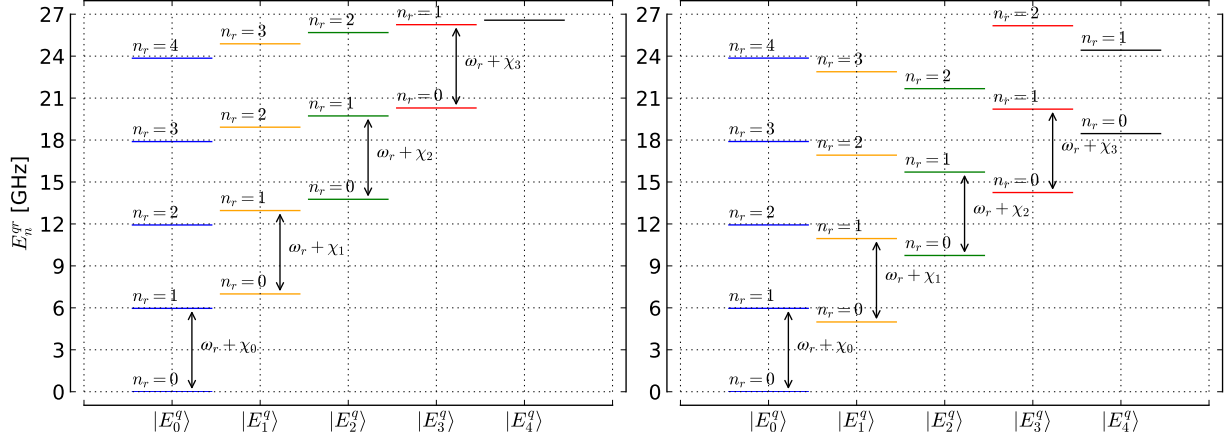


Figure 1.16: Energy level diagrams for the transmon-resonator system in the sweet spot when the detuning $\Delta\omega = \omega_r - \omega_{ge}$ is negative (right) or positive (left).

In Fig. 1.16 the energy structure of the compound system in the sweet-spot ($\Phi_{ext} = 0$) is shown for two cases of positive and negative detuning. The dispersively shifted frequencies can be calculated from perturbation theory. For example, for the transition $|0, g\rangle \rightarrow |1, g\rangle$ the shift is defined to the second order as

$$\begin{aligned} \chi_0 &= E_{1g}^{(1)} + E_{1g}^{(2)} - E_{0g}^{(1)} - E_{0g}^{(2)} \\ &= \langle 1, g | \hat{\mathcal{H}}_i | 1, g \rangle + \sum_{i, \alpha \neq 1, g} \frac{|\langle g, 1 | \hat{\mathcal{H}}_i | i, \alpha \rangle|^2}{E_{1g} - E_{i\alpha}} \\ &\quad - \langle 0, g | \hat{\mathcal{H}}_i | 0, g \rangle - \sum_{i, \alpha \neq 0, g} \frac{|\langle g, 0 | \hat{\mathcal{H}}_i | i, \alpha \rangle|^2}{E_{1g} - E_{i\alpha}}. \end{aligned}$$

As long as $\hat{\mathcal{H}}_i$ mixes only adjacent resonator states the first order corrections vanish, and so do the summations over i : $\sum_{i, \alpha} \rightarrow \sum_{0, \alpha} + \sum_{2, \alpha} (\sum_{1, \alpha})$. These sums then can be further truncated:

$$E_{1g}^{(2)} - E_{0g}^{(2)} \approx \frac{|\langle g, 1 | \hat{\mathcal{H}}_i | 0, e \rangle|^2}{\omega_r - \omega_{ge}} + \frac{|\langle g, 1 | \hat{\mathcal{H}}_i | 2, e \rangle|^2}{\omega_r - 2\omega_r - \omega_{ge}} - \frac{|\langle g, 0 | \hat{\mathcal{H}}_i | 1, e \rangle|^2}{-\omega_r - \omega_{ge}} \quad (1.2.5)$$

due to the selection rule of \hat{n} : $\langle E_n^q | \hat{n} | E_{n+2k}^q \rangle = 0$, $k \in \mathbb{Z}$ and the fast (exponential from numerics) decay of its matrix elements over distance between transmon energy eigenstates (see subsection 1.2.2). It can be easily proven that last two elements of (1.2.5) are equal up to the factor of $\sqrt{2}^2$ and final equation for χ_0 follows

$$\chi_0 = g^2 \left[\frac{n_{ge}^2}{\omega_r - \omega_{ge}} - \frac{n_{ge}^2}{\omega_r + \omega_{ge}} \right]. \quad (1.2.6)$$

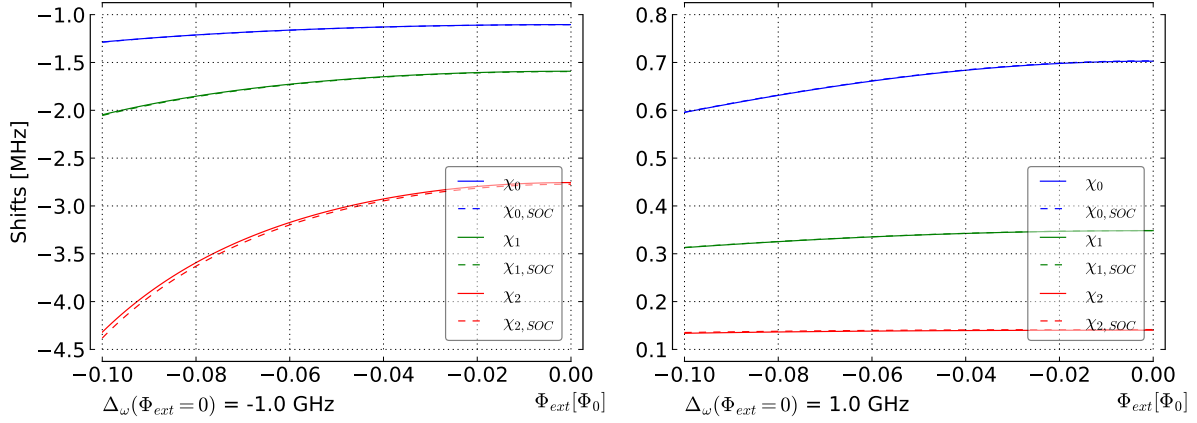


Figure 1.17: Dispersive shifts for the first three states of the transmon in dependence on the external flux. Solid lines are numerical solution and dashed lines are results from equations (1.2.6)-(1.2.8).

Similarly, dispersive shifts for the other two transmon states are derived:

$$\chi_1 = g^2 \left[\frac{n_{ef}^2}{\omega_r - \omega_{ef}} - \frac{n_{ef}^2}{\omega_r + \omega_{ef}} + \frac{n_{eg}^2}{\omega_r + \omega_{ge}} - \frac{n_{eg}^2}{\omega_r - \omega_{ge}} \right], \quad (1.2.7)$$

$$\chi_2 = g^2 \left[\frac{n_{fd}^2}{\omega_r - \omega_{fd}} - \frac{n_{fd}^2}{\omega_r + \omega_{fd}} + \frac{n_{fe}^2}{\omega_r + \omega_{ef}} - \frac{n_{fe}^2}{\omega_r - \omega_{ef}} \right], \quad (1.2.8)$$

where g, e, f, d denote the first 4 energy eigenstates of the transmon, $n_{\alpha\beta} = \langle \alpha | \hat{n} | \beta \rangle$ is the matrix element of \hat{n} and $g = |\frac{\hat{\mathcal{H}}_i}{i(\hat{a}^\dagger - \hat{a}) \otimes \hat{n}}|$ is the coupling parameter which precedes the operator part in the interaction Hamiltonian. In Fig. 1.17 these formulas are compared to the numerical solution. As can be seen, the analytical solution is quite accurate at the detunings of about 1 GHz. Note that dispersive shift χ_1 is always smaller than χ_0 when the detuning is large enough meaning that the resonator frequency will move down from its initial position. There is also another regime which occurs when the resonator frequency is situated between transitions ge and ef and is called *straddling regime* by Koch et al.⁵ The dispersive regime breaks down there when the coupling is strong enough (i.e., 50 MHz) and the anharmonicity of the qubit is not very large (i.e., 200 MHz) compared to it, so the second order correction equations become inaccurate. In this regime, however, $\chi_1 > \chi_0$, and the resonator moves up when the qubit is excited.

1.3 Dynamics

1.3.1 Driving of an isolated transmon

To simulate the dynamics in the unitary case without taking into account the dissipative processes it is enough to solve the Schrödinger equation with the Hamiltonian (1.2.3) summed with the driving part (1.2.4). The final state after some time of the evolution t will be

described with a Dyson series or a \hat{T} -exponent:

$$\begin{aligned} |\psi(t)\rangle &= \hat{T} \exp \left\{ -\frac{i}{\hbar} \left(\hat{\mathcal{H}}_{tr} t + \int_0^t \hat{\mathcal{H}}_q^d(\tau) d\tau \right) \right\} |\psi(0)\rangle \\ &\equiv \hat{U}(t, 0) |\psi(0)\rangle \equiv \sum_k c_k(t) |E_k^q\rangle, \end{aligned} \quad (1.3.1)$$

where $|E_k^q\rangle$ denotes the k 's eigenstate of the qubit Hamiltonian and $\hat{U}(t, 0)$ is the standard evolution operator. There is no exact analytical solution for $c_k(t)$ for the transmon qubit, so we will use some approximations, perturbation theory and numerical methods to get an insight into the dynamics of this quantum system.

Approximate solution for two-level dynamics

Let's write down the matrix equation for the time-dependent Schrödinger's equation in the energy representation of the transmon:

$$i\hbar \begin{pmatrix} \dot{c}_g \\ \dot{c}_e \\ \dot{c}_f \\ \dot{c}_d \\ \vdots \end{pmatrix} = \left[\begin{pmatrix} E_g & 0 & 0 & 0 & \cdots \\ 0 & E_e & 0 & 0 & \cdots \\ 0 & 0 & E_f & 0 & \cdots \\ 0 & 0 & 0 & E_d & \cdots \\ \vdots & \vdots & \vdots & \vdots & \ddots \end{pmatrix} + f(t) \begin{pmatrix} 0 & n_{ge} & 0 & n_{gd} & \cdots \\ n_{eg} & 0 & n_{ef} & 0 & \cdots \\ 0 & n_{fe} & 0 & n_{fd} & \cdots \\ n_{dg} & 0 & n_{df} & 0 & \cdots \\ \vdots & \vdots & \vdots & \vdots & \ddots \end{pmatrix} \right] \begin{pmatrix} c_g \\ c_e \\ c_f \\ c_d \\ \vdots \end{pmatrix}. \quad (1.3.2)$$

Here we have used the properties of the \hat{n} (see subsection 1.2.2) operator to simplify its matrix representation. Now we can write down the differential equations for three lowest levels:

$$\begin{cases} i\hbar \dot{c}_g = E_g c_g + f(t)(n_{ge} c_e + n_{gd} c_d + \cdots), \\ i\hbar \dot{c}_e = E_e c_e + f(t)(n_{eg} c_g + n_{ef} c_f + \cdots), \\ i\hbar \dot{c}_f = E_f c_f + f(t)(n_{fe} c_e + n_{fd} c_d + \cdots). \end{cases} \quad (1.3.3)$$

Then we use the following ansatz: $c_\alpha = c'_\alpha \exp(-i\frac{E_\alpha t}{\hbar})$, which transforms the Hamiltonian into the *rotating frame*. In this frame, the unperturbed Hamiltonian is equal to $\hat{0}$, and the equations (1.3.3) become (omitting apostrophes):

$$\begin{cases} i\hbar \dot{c}_g = f(t)(n_{ge} c_e e^{-i\omega_{ge} t} + n_{gd} c_d e^{-i\omega_{gd} t} + \cdots), \\ i\hbar \dot{c}_e = f(t)(n_{eg} c_g e^{i\omega_{ge} t} + n_{ef} c_f e^{-i\omega_{ef} t} + \cdots), \\ i\hbar \dot{c}_f = f(t)(n_{fe} c_e e^{i\omega_{ef} t} + n_{fd} c_d e^{-i\omega_{df} t} + \cdots). \end{cases}$$

Finally, assuming harmonic perturbation at ge transition frequency, $f(t) = \hbar f \cos(\omega t + \phi) = \frac{\hbar f}{2}(e^{i\omega_{ge} t + i\phi} + e^{-i\omega_{ge} t - i\phi})$, and dropping all oscillating terms (*rotating wave approximation, RWA*) we obtain the standard two-level dynamics for Rabi oscillations around the axis $-\phi$ degrees away from the x -axis of the Bloch sphere with $\Omega_R = f n_{ge}$:

$$\begin{cases} i\hbar \dot{c}_g = \frac{\hbar f e^{i\phi}}{2} n_{ge} c_e, \\ i\hbar \dot{c}_e = \frac{\hbar f e^{-i\phi}}{2} n_{eg} c_g. \end{cases} \Leftrightarrow i\partial_t |\psi(t)\rangle = \frac{\Omega_R}{2} [\cos(\phi) \hat{\sigma}_x - \sin(\phi) \hat{\sigma}_y] |\psi(t)\rangle. \quad (1.3.4)$$

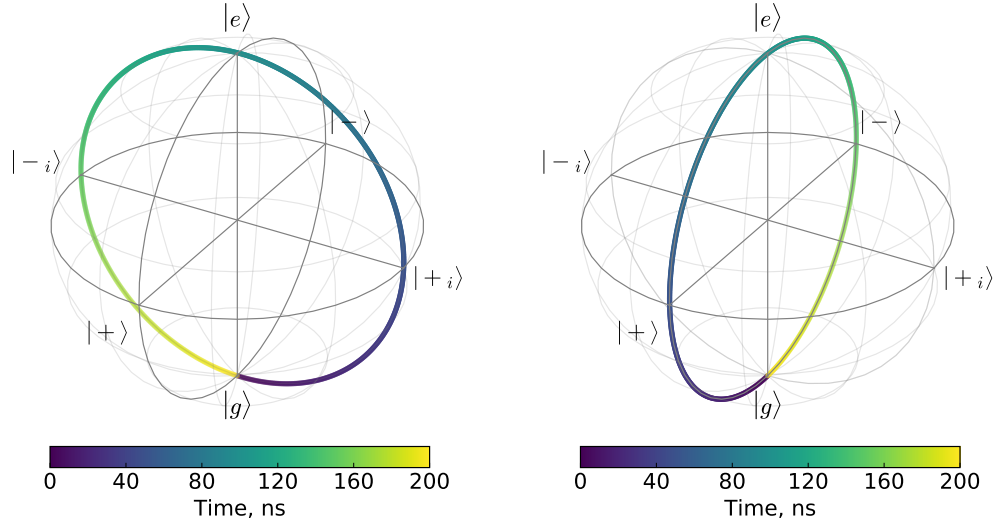


Figure 1.18: Visualization of the solution of (1.3.4) on the Bloch sphere for $\Omega_R = 5$ MHz and two values of ϕ : 0 (left) and $-\pi/2$ (right).

The exact solution for this equation may be obtained with use of the matrix exponent and the following properties of $\hat{\sigma}_{x,y}$: $\hat{\sigma}_x^2 = \hat{\mathbb{1}}$, $\hat{\sigma}_x^3 = \hat{\sigma}_x$. However, since $\hat{\sigma}_x$ and $\hat{\sigma}_y$ are not commuting, it is a bit cumbersome to calculate the matrix exponent when ϕ is arbitrary, and it's easier just to switch the basis so that $\phi = 0$. So below we solve the equation in this case:

$$\begin{aligned} |\psi(t)\rangle &= \exp\left\{i\frac{\Omega_R}{2}\hat{\sigma}_x t\right\}|\psi(0)\rangle \\ &= \left[\hat{\mathbb{1}} \cos\left(\frac{\Omega_R}{2}t\right) + i\hat{\sigma}_x \sin\left(\frac{\Omega_R}{2}t\right)\right]|\psi(0)\rangle. \end{aligned} \quad (1.3.5)$$

With initial state $|g\rangle$, we can calculate the probability of being in the states $|e\rangle$ and $|+\rangle = \frac{1}{\sqrt{2}}(|g\rangle + |e\rangle)$ to be as follows:

$$\begin{aligned} P(|e\rangle)(t) &= |\langle e|\psi(t)\rangle|^2 = \frac{1 - \cos(\Omega_R t)}{2}, \\ P(|+\rangle)(t) &= |\langle +|\psi(t)\rangle|^2 = \frac{1}{2}. \end{aligned} \quad (1.3.6)$$

Clearly, this is by definition the rotation around the x -axis. The y rotation may be derived in a similar way if the phase is chosen to be $-\pi/2$.

In general, using these formulas, we can define $(\theta)^{x(y)}$ -pulse as windowed sine wave with window of correct amplitude, duration and phase, so that the qubit is rotated θ radians around the corresponding axis (see Fig. 1.18). For example, for a fixed-length pulse of t_g , the $(-\frac{\pi}{2})^y$ -pulse amplitude f_q should be $-\pi/2t_g n_{ge}$ and pulse phase ϕ equal to $-\pi/2$. Conversely, for a fixed Ω_R (drive amplitude f_q) to perform the same rotation the pulse time t_g should be chosen as $\pi/2\Omega_R$ for the excitation signal with the phase increased by π (as $t_g \geq 0$).

Time-dependent perturbation theory

Perturbation theory allows semianalytical calculation of the transition rates (Rabi oscillation frequencies) for single and multi-photon processes. Using the the Dyson series we can write down the expansion of the evolution operator $\hat{U}(t, t_0)$ and then use it to calculate the expansion of the transition rate $A_{fi} = \langle f | \hat{U}(t, t_0) | i \rangle$ from some initial state $|i\rangle$ to the final state $|f\rangle$ under some driving operator $\hat{V}(t)$. Here is the result for the $\hat{U}(t, t_0)$ decomposition:¹⁶

$$\begin{aligned} \hat{U}(t, t_0) &= 1 + \sum_n \hat{U}^{(n)}(t, t_0), \\ \hat{U}^{(n)}(t, t_0) &= \left(-\frac{i}{\hbar}\right)^n \int_{t_0}^t dt_1 \hat{V}_I(t_1) \int_{t_0}^{t_1} dt_2 \hat{V}_I(t_2) \cdots \int_{t_0}^{t_{n-1}} dt_n \hat{V}_I(t_n), \end{aligned} \quad (1.3.7)$$

where $\hat{V}_I(t) = \exp(i\hat{\mathcal{H}}_{tr}(t - t_0)/\hbar) \hat{V}(t) \exp(-i\hat{\mathcal{H}}_{tr}(t - t_0)/\hbar)$ is the driving operator in the interaction picture (same as in the rotating frame). For example, let's reproduce the previous result and calculate the Rabi frequency for the single-photon transition. The transition rate $A_{eg}^{(1)}(t) = \langle e | \hat{U}^{(1)}(t, t_0) | g \rangle$ when $\hat{V}(t) = \hbar f \hat{n} \cos(\omega t)$ is calculated as follows :

$$A_{eg}^{(1)}(t) = -i \frac{f n_{eg}}{2} \int_{t_0}^t e^{i\omega_{ge}t_1} (e^{i\omega t_1} + e^{-i\omega t_1}) dt_1. \quad (1.3.8)$$

In the limit of $t - t_0 \gg 1/\omega$ and $\omega - \omega_{ge} \ll 1$ this can be rewritten as

$$A_{eg}^{(1)}(t) \sim -i \frac{f n_{eg}}{2} t.$$

Consequently, $P(|e\rangle) = |A_{eg}|^2 = (f n_{eg}/2)^2 t^2$, and this is exactly the first term of the expansion of the first formula in (1.3.6) thus giving us the same Rabi frequency of $f n_{eg}$.

Multi-photon transition rates are harder to calculate since they require summations over different intermediate states $|j\rangle$ between the initial and the final state. Nevertheless, below we will calculate the Rabi frequency of the two-photon $gf/2$ transition, so that $\omega \approx \omega_{gf}/2$. The first order correction vanishes for this transition, and thus we need to calculate the second order correction only. Following Faisal,¹⁶ we obtain:

$$A_{fg}^{(2)}(t) \sim i(f/2)^2 \sum_j \frac{n_{fj} n_{jg}}{\omega_{gj} - \omega_{gf}/2} t \approx i(f/2)^2 \frac{n_{fe} n_{eg}}{\omega_{ge} - \omega_{gf}/2} t.$$

Analogously to the previous case, this gives us the two-photon Rabi frequency:

$$\Omega_{R,gf}^{2p} = \frac{f^2 n_{fe} n_{eg}}{|\alpha|}, \quad (1.3.9)$$

where α is the anharmonicity of the transmon. Note that it is proportional to the squared drive strength – a standard result for a 2-photon process. This formula will be tested numerically in the section below.

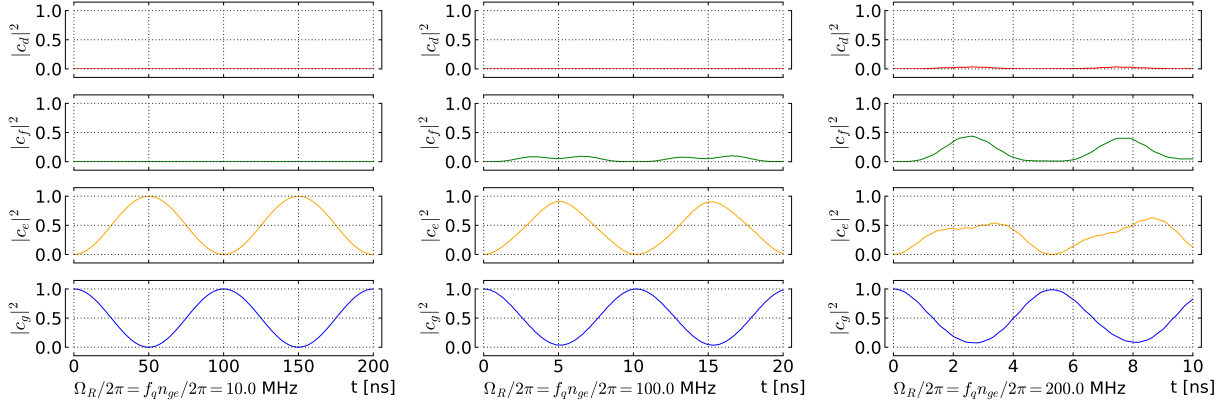


Figure 1.19: Dynamics of the isolated driven transmon qubit with different drive strengths $f_q/2\pi = 0.01\text{--}0.2$ GHz, where f_q is an effective amplitude of the drive (1.2.4) $f_q(t) = \hbar f_q \cos(\omega_{ge}t)$. It can be seen that significant distortions and leakage to higher levels occur when amplitude becomes comparable to the transmon's anharmonicity.

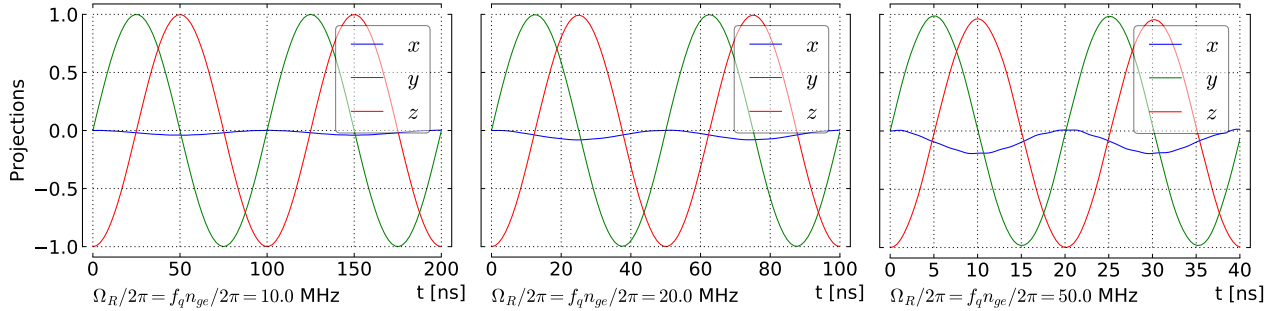


Figure 1.20: Numerical solution for the two-level behaviour of the transmon in the computational basis for different drive strengths. Note the phase error due to the leakage to the higher levels which is growing with the driving strength and is noticeable even when the drive strength is small compared to the anharmonicity.

Numerical solution for two-level dynamics

The simulation of the transmon dynamics can be performed as a standard numerical linear ODE solution which is also possible within QuTiP framework using the *mesolve* routine. Below the results for the following model will be presented:

$$\hat{\mathcal{H}} = \hat{\mathcal{H}}_{tr} + \hat{\mathcal{H}}_q^d(t), \quad f_q^d(t) = \hbar f_q \cos(\omega_{ge}t), \quad \omega_{ge}/2\pi = 6 \text{ GHz}, \quad \alpha/2\pi = -200 \text{ MHz}.$$

We can solve the time-dependent Schrödinger equation with this Hamiltonian with $|g\rangle$ as the initial state to obtain system state as each time point $|\psi(t)\rangle$ we wish, and then calculate the projections of these states onto the eigenstates to find decomposition coefficients $c_{g..c_d}$. Alternatively, it is possible to find the expectation values for the quasi-two-level operators

$$\hat{\sigma}_x = |g\rangle\langle e| + |e\rangle\langle g|, \quad \hat{\sigma}_y = i|g\rangle\langle e| - i|e\rangle\langle g|, \quad \hat{\sigma}_z = |e\rangle\langle e| - |g\rangle\langle g|$$

for each state $|\psi(t)\rangle$ which allow us to find its phase in the *computational basis*. However, when higher levels are involved in the dynamics, these expectation values lose their meaning

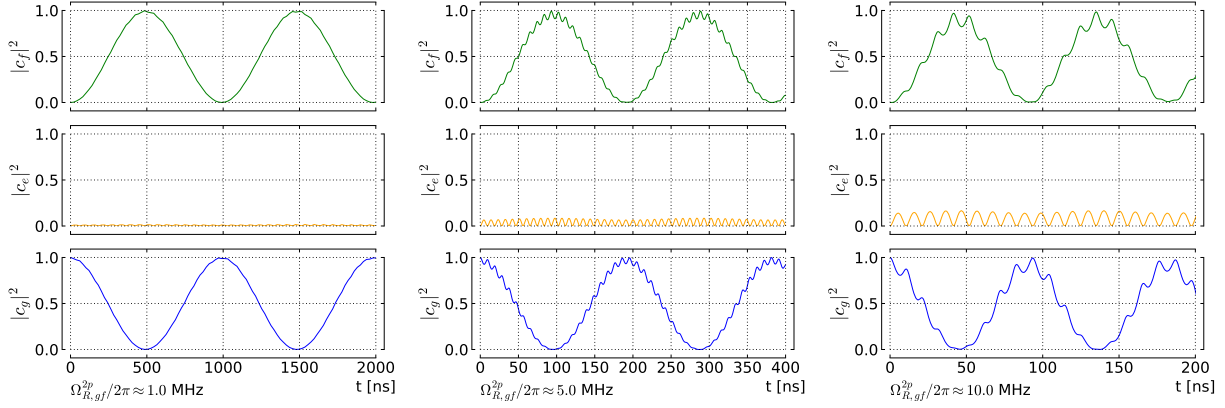


Figure 1.21: Simulated two-photon $gf/2$ Rabi oscillations. The Rabi frequency is closer to the theoretically predicted one in (1.3.9) when the drive is weak and deviates more and more when the drive strength is increased. Higher-frequency oscillations are present, too and also grow in amplitude.

and should be used with discretion.

The result of such simulations can be observed in Fig. 1.19 and Fig. 1.20. As one can see, when the driving amplitude becomes comparable to the anharmonicity of the transmon, significant leakage to higher states occurs which in the computational basis manifests itself as a phase error. This error is significant even when the driving strength is relatively small, so special techniques such as Derivative Removal by Adiabatic Gate^{17,18} (DRAG) or Half Derivative¹⁹ (HD) method were suggested to cope with it.

DRAG procedure can correct any continuous pulse rotating the qubit around some axis (i.e., $(\pi)^x$) by adding two simultaneous pulses around two other axes. If the $(\pi)^x$ -pulse has the windowing function $F_x(t)$, the pulses around y -axis and z -axis (which is usually just a DC-pulse, i.e. with no carrier, providing dynamic detuning of the qubit during the) should be constructed as follows:

$$F_y = -\frac{\dot{F}_x}{\alpha}, \quad \omega - \omega_{ge}(t) = \frac{(\lambda^2 - 4)F_x^2}{4\alpha}$$

However, it is possible to alleviate the necessity of z -pulses by putting $F_y = -\frac{1}{2}\frac{\dot{F}_x}{\alpha}$. This change significantly reduces the complexity of the original DRAG operation while maintaining approximately the same performance, as numerical simulations has shown.¹⁹ The resulting operation is named Half Derivative method after the factor of $1/2$ before \dot{F}_x , and not because it is somehow connected to fractional calculus.

Numerical solution for two-photon dynamics

Similarly to the single-photon two-level process simulated above, we can simulate the two-photon transition $gf/2$. To test the equation (1.3.9), we put f_q which is the amplitude

of the two-photon driving $f_q \cos(\omega_{fg}/2 + t)$ to be as follows:

$$f_q = \sqrt{\frac{\Omega_{R,gf}^{2p} |\alpha|}{n_{ge} n_{ef}}},$$

where $\Omega_{R,gf}^{2p}$ is the two-photon Rabi frequency which we want to observe. For $\Omega_{R,gf}^{2p}/2\pi = 1$ MHz (5 MHz, 10 MHz), we observe the two-photon Rabi frequency of 1.03 MHz (5.2 MHz, 11 MHz) which is a good match concerning the perturbative nature of the equation (1.3.9). The results of the numerical simulation are presented in Fig. 1.21.

1.3.2 Relaxation dynamics (driven and undriven)

The relaxation process for the transmon is simulated using a Lindbladian master equation with a following dissipative operator:

$$\hat{c} = \sum_{j \geq 0}^{\infty} \frac{n_{j,j+1}}{n_{01}} |j\rangle \langle j+1| \quad (1.3.10)$$

which is from the definition a lowering operator. It becomes the annihilation operator of the standard harmonic oscillator in the limit of very large E_J/E_C , so it's a good operator use for modelling of the relaxation channel. For a deeper review on this see L.S. Bishop's thesis.¹⁰

The dynamics of the dissipative transmon then will be governed by the following equation:

$$\frac{\partial}{\partial t} \hat{\rho}_q = \frac{i}{\hbar} [\hat{\rho}_q, \hat{\mathcal{H}}_q + \hat{\mathcal{H}}_q^d(t)] + \gamma \mathcal{D}[\hat{c}] \hat{\rho}_q, \quad (1.3.11)$$

where $\mathcal{D}[\hat{O}] \hat{\rho}_q = \hat{O} \hat{\rho}_q \hat{O}^\dagger - \frac{1}{2} \{ \hat{O}^\dagger \hat{O}, \hat{\rho}_q \}$ and γ is the relaxation rate. Pure dephasing may also be added in a similar way.

Below the dynamics of the undriven relaxation and excitation with strong driving are presented as examples of the solution of (1.3.11).

1.3.3 Linewidth dependence on drive power

Knowing the way to model the relaxation of the qubit it's possible to compare the relaxation rate with the linewidth of the qubit on the population graph. The way is to simulate the evolution until the steady state is reached for all driving frequencies around the resonance, calculate populations of the excited state for each reached steady state and then measure the width at the half-maximum of the resulting peak. However, for two-level dynamics the linewidth $\delta\omega$ depends on the driving power as the Rabi oscillations are induced between the levels. So for correct determination of the linewidth it's necessary to measure the linewidth at low driving amplitudes.

Before demonstrating the numerical results for the transmon qubit, a brief analytical solution for the problem in the case of a two-level system will be shown. The master equation

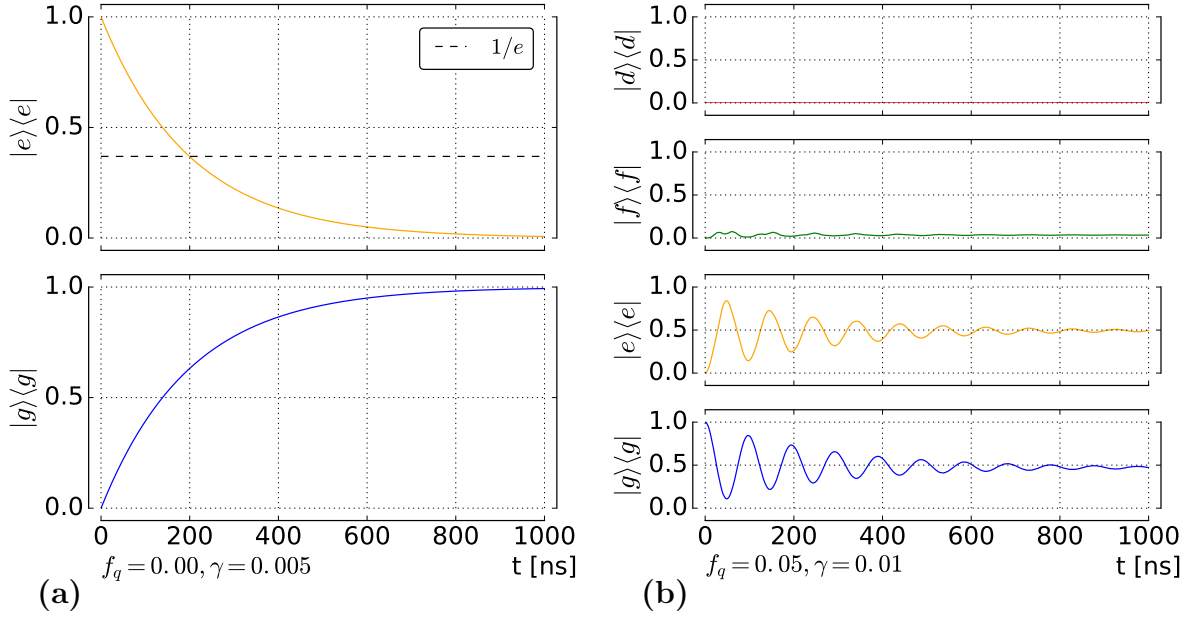


Figure 1.22: Behaviour of the equation (1.3.11), represented as populations of the eigenstates depending on time. **(a)** Relaxation of the first excited state without any driving. The population reaches $1/e$ in $1/\gamma$ ns, as expected. **(b)** Excitation of the ground state into the steady state which is an incoherent mixture of the first three states. Driving is resonant with ge transition of the transmon.

for this problem is as follows (within RWA):

$$\frac{\partial}{\partial t} \hat{\rho}_{t|s} = \frac{i}{\hbar} [\hat{\rho}_{t|s}, \frac{\hbar \overbrace{(\omega_{t|s} - \omega_d)}^{\Delta\omega}}{2} \hat{\sigma}_z + \frac{\hbar \Omega_R}{2} \hat{\sigma}_x] + \gamma \mathcal{D}[\hat{\sigma}^-] \hat{\rho}_{t|s}.$$

Knowing that $\text{Tr}[\hat{\rho}_{t|s}] = 1$ and that $\hat{\rho}_{t|s} = \hat{\rho}_{t|s}^\dagger$ we can write down three ODEs from this master equation:

$$\begin{aligned} \frac{d}{dt} \rho_{11}(t) &= -\gamma \rho_{11}(t) + i \left(\frac{\Omega_R}{2} \rho_{12}(t) - \frac{\Omega_R}{2} \rho_{21}(t) \right), \\ \frac{d}{dt} \rho_{12}(t) &= -\frac{\gamma}{2} \rho_{12}(t) + i \left(\frac{\Omega_R}{2} \rho_{11}(t) - \frac{\Omega_R}{2} (1 - \rho_{11}(t)) - \Delta\omega \rho_{12}(t) \right), \\ \rho_{21}(t) &= \rho_{12}^\dagger(t). \end{aligned}$$

It is practical for our case to solve these equations for steady state, when $\frac{\partial}{\partial t} \hat{\rho}_{t|s} = 0$. The matrix elements then are

$$\rho_{11} = \frac{\Omega_R^2}{2\Omega_R^2 + \gamma^2 + 4\Delta\omega^2}, \quad \rho_{12} = -\frac{\Omega_R(i\gamma + 2\Delta\omega)}{2\Omega_R^2 + \gamma^2 + 4\Delta\omega^2}, \quad \rho_{21} = \frac{\Omega_R(i\gamma - 2\Delta\omega)}{2\Omega_R^2 + \gamma^2 + 4\Delta\omega^2}.$$

From here it is easy to find the analytical linewidth at half maximum of the $\rho_{11}(\omega_d)$:

$$\delta\omega = \sqrt{2\Omega_R^2 + \gamma^2}.$$

When the $\Omega_R \rightarrow 0$, $\delta\omega \rightarrow \gamma$, and thus it is possible to extract T_1 in case of absence of pure dephasing or at least to put a lower bound on it if the pure dephasing is present. It is important to notice that in the experiment the measured frequency is expressed in Hz though $\delta\omega$ is in rad/s. Therefore, the experimental linewidth should be, firstly, measured at very low powers and, secondly, multiplied by 2π to obtain γ . In the presence of pure dephasing the formula for $\delta\omega$ becomes a bit more complicated, but also can be straightforwardly calculated with use of Computer Algebra Systems:

$$\delta\omega_{\text{with dephasing}} = \sqrt{2\Omega_R^2(1 + 2\gamma_\phi/\gamma) + (\gamma + 2\gamma_\phi)^2} \xrightarrow{\Omega_R \rightarrow 0} \gamma + 2\gamma_\phi.$$

Interestingly enough, if there's no relaxation and $\gamma = 0$, the formula shows divergence of the linewidth. This happens because the solution of the master equation in this case yields $\rho_{11} = 1/2$ in the steady state, independent of the driving detuning and driving strength, and thus the linewidth can't at all be defined.

For the transmon, the two-level dynamics between its ground and first excited state is equivalent; however, there's no simple analytical solution for the dynamics. To see the behaviour is same in this case we have to resort to numerical modelling (see Fig. 1.23). As can be seen, the linewidth $\delta\omega$ grows with the increased power, and, in contrast, saturates at low powers, reaching the value of γ .

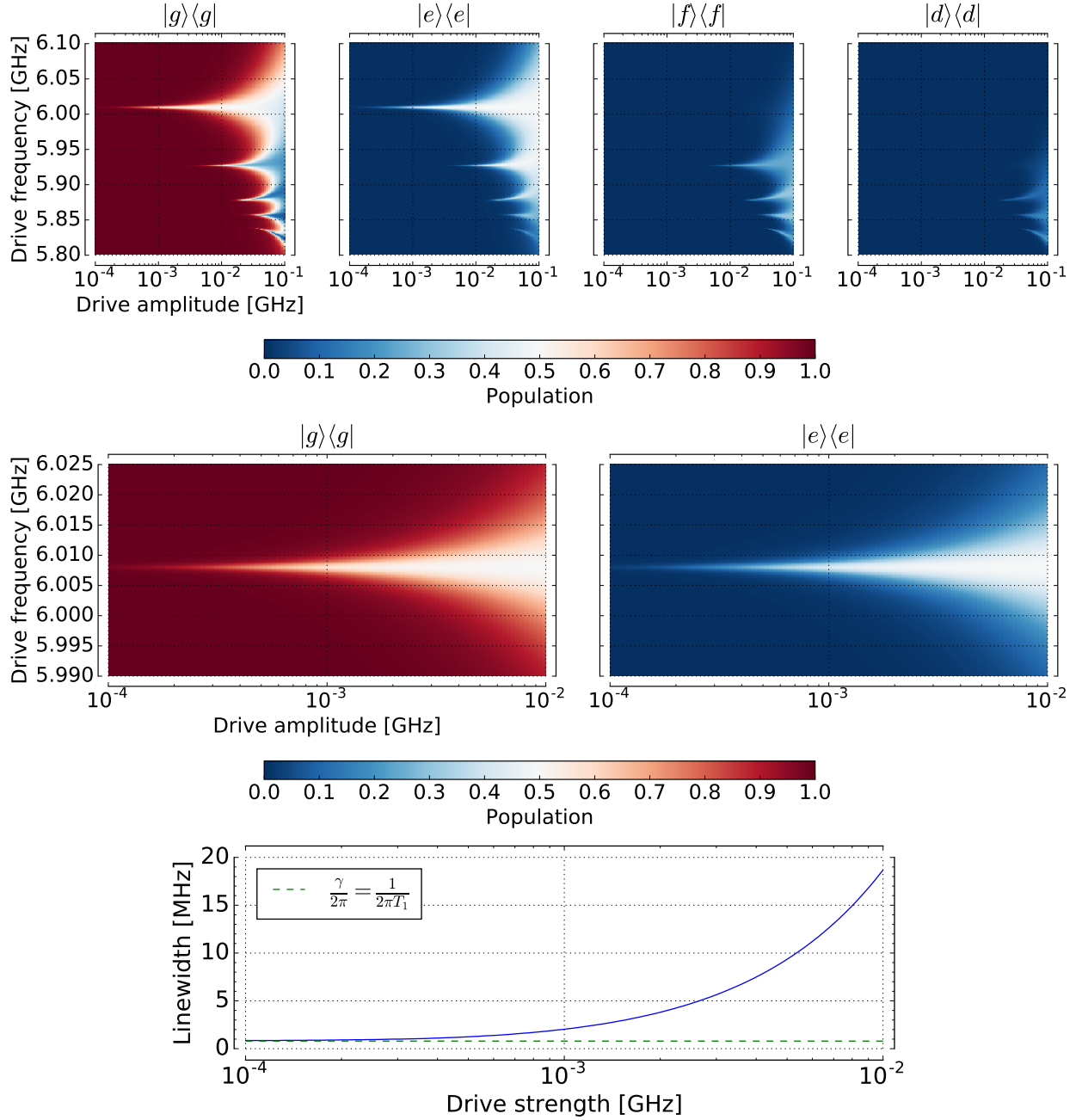


Figure 1.23: Linewidth analysis in dependence on the driving power f_q for $\gamma = 5 \text{ rad}/\mu\text{s}$. As can be seen, with the increasing drive amplitude the spectral line becomes wider. In contrast, its width levels off when the amplitude is decreased, and reaches asymptotically the value of $\frac{\gamma}{2\pi}$. The factor 2π appears as the linewidth found in the experiment usually is in Hz, but the equality that holds is that $\gamma = \delta\omega$, and $\delta\omega = 2\pi\delta\nu$.

Bibliography

- ¹ Coplanar waveguide resonators for circuit quantum electrodynamics / M. Göppl, A. Fragner, M. Baur et al. // Journal of Applied Physics. — 2008. — Vol. 104, no. 11. — P. 1–8. — 0807.4094. (referenced on p. [4 and 7])
- ² Pozar D. M. Microwave Engineering, copyright 2012 by John Wiley & Sons. — Inc. (referenced on p. [4, 6 and 8])
- ³ Kiselev E. Design and Measurement of Superconducting Spiral Microwave Resonators : Ph.D. thesis / E. Kiselev. — 2013. (referenced on p. [6])
- ⁴ Efficient and robust analysis of complex scattering data under noise in microwave resonators / S Probst, FB Song, PA Bushev et al. // Review of Scientific Instruments. — 2015. — Vol. 86, no. 2. — P. 024706. (referenced on p. [9])
- ⁵ Charge insensitive qubit design derived from the Cooper pair box / J. Koch, Terri M. Yu, Jay M. Gambetta et al. — 2007. — P. 21. — 0703002. (referenced on p. [12, 13, 14, 15, 17 and 19])
- ⁶ The flux qubit revisited / F Yan, S Gustavsson, A Kamal et al. // Preprint at <http://arxiv.org/abs/1508.06299>. — 2015. (referenced on p. [12])
- ⁷ Observation of high coherence in Josephson junction qubits measured in a three-dimensional circuit QED architecture / Hanhee Paik, DI Schuster, Lev S Bishop et al. // Physical Review Letters. — 2011. — Vol. 107, no. 24. — P. 240501. (referenced on p. [12])
- ⁸ Coherent Josephson qubit suitable for scalable quantum integrated circuits / Rami Barends, Julian Kelly, Anthony Megrant et al. // Physical review letters. — 2013. — Vol. 111, no. 8. — P. 080502. (referenced on p. [13])
- ⁹ Devoret M. H. Quantum fluctuations in electrical circuits // Les Houches, Session LXIII. — 1995. — URL: <http://www.physique.usherb.ca/tremblay/cours/PHY-731/Quantum{ }circuit{ }theory-1.pdf>. (referenced on p. [13 and 16])
- ¹⁰ Bishop L. S. Circuit Quantum Electrodynamics. — 2010. — P. 168. — 1007.3520. (referenced on p. [15 and 25])
- ¹¹ Cavity quantum electrodynamics for superconducting electrical circuits: an architecture for quantum computation / Alexandre Blais, Ren-Shou Huang, Andreas Wallraff et al. — 2004. — P. 14. — 0402216. (referenced on p. [15])

- ¹² Coupling superconducting qubits via a cavity bus / J Majer, JM Chow, JM Gambetta et al. // *Nature*. — 2007. — Vol. 449, no. 7161. — P. 443–447. (referenced on p. [15])
- ¹³ Antibunching of microwave-frequency photons observed in correlation measurements using linear detectors / D Bozyigit, C Lang, L Steffen et al. // *Nature Physics*. — 2011. — Vol. 7, no. 2. — P. 154–158. (referenced on p. [15])
- ¹⁴ Bader S. *The Transmon Qubit Theory*. — 2013. (referenced on p. [15])
- ¹⁵ Johansson J. R., Nation P. D., Nori F. QuTiP: An open-source Python framework for the dynamics of open quantum systems. — 2011. — 1110.0573v2. (referenced on p. [17])
- ¹⁶ Faisal Farhad HM. *Theory of multiphoton processes*. — Springer Science & Business Media, 2013. (referenced on p. [22])
- ¹⁷ Simple Pulses for Elimination of Leakage in Weakly Nonlinear Qubits / F. Motzoi, J. M. Gambetta, P. Rebentrost, F. K. Wilhelm // *Physical Review Letters*. — 2009. — Vol. 103, no. 11. — P. 1–4. — 0901.0534. (referenced on p. [24])
- ¹⁸ Optimized driving of superconducting artificial atoms for improved single-qubit gates / J. M. Chow, L. Dicarlo, J. M. Gambetta et al. // *Physical Review A - Atomic, Molecular, and Optical Physics*. — 2010. — Vol. 82, no. 4. — P. 2–5. — 1005.1279. (referenced on p. [24])
- ¹⁹ Reduced phase error through optimized control of a superconducting qubit / Erik Lucero, Julian Kelly, Radoslaw C. Bialczak et al. // *Physical Review A - Atomic, Molecular, and Optical Physics*. — 2010. — Vol. 82, no. 4. — P. 1–7. — 1007.1690. (referenced on p. [24])
- ²⁰ Sank D. T. *Fast, Accurate State Measurement in Superconducting Qubits* : Ph. D. thesis / D. T. Sank. — 2014.
- ²¹ Improving the coherence time of superconducting coplanar resonators / H Wang, M Hofheinz, J Wenner et al. // *Applied Physics Letters*. — 2009. — Vol. 95, no. 23. — P. 233508.
- ²² Nonlinear response of the vacuum Rabi resonance / Lev S Bishop, JM Chow, Jens Koch et al. // *Nature Physics*. — 2009. — Vol. 5, no. 2. — P. 105–109.
- ²³ Dynamical decoupling and noise spectroscopy with a superconducting flux qubit / Jonas Bylander, Simon Gustavsson, Fei Yan et al. // *Nature Physics*. — 2011. — Vol. 7, no. 7. — P. 21. — 1101.4707.
- ²⁴ Preskill J. Notes on noise. — URL: http://www.theory.caltech.edu/people/preskill/papers/decoherence_notes.pdf.
- ²⁵ Zurek Wojciech Hubert. *Decoherence, einselection, and the quantum origins of the classical* // *Reviews of Modern Physics*. — 2003. — Vol. 75, no. 3. — P. 715–775. — 0105127.